



Dynamic Analysis of the Tensegrity Structure of a Rotary Airborne Wind Energy Machine

Gonzalo Sánchez-Arriaga ¹, Álvaro Cerrillo-Vacas ¹, Daniel Unterweger ², and Christof Beaupoil ²

¹Aerospace Engineering Department, Universidad Carlos III de Madrid, Avda de la Universidad 30, 28911, Leganes, Spain

²SomeAWE Labs S.L, Calle Edil Marina Olcina 7, 03540 Alicante, Spain

Correspondence: Gonzalo Sánchez-Arriaga (gonzalo.sanchez@uc3m.es)

Abstract. The dynamic behavior of the tensegrity structure (helix) of a Rotary Wind Energy (RAWE) machine was investigated by combining experimental and numerical techniques. Taking advantage of the slenderness of the helix, a dynamic model for the evolution of its center line and the torsional deformation was developed by using Cosserat theory. The constitutive relations for the axial, bending and torsional stiffness, which are a fundamental component of the model, were obtained experimentally by carrying out laboratory tests. Three scenarios of increasing complexity were then studied with the numerical tool. Firstly, a stationary solution of the model, i.e. with fixed ends and no rotation, was found numerically and used to verify the correct implementation of a numerical code based on finite elements. The stability analysis of this solution, which corresponds to the state of the structure just after deployment but before operation, showed that the natural periods of longitudinal, lateral, and torsional modes of the RAWE structure under consideration are around 0.03 s, 0.2 s and 0.4 s, respectively. Secondly, the dynamic in nominal operation was investigated by keeping fixed both end tips and implementing a controller that adjusts the torque at the ground to reach a target angular velocity of 120 rpm. Key characteristic variables like the tension and the response times of the helix were obtained. Thirdly, the dynamic of the helix when the lower end is fixed and the upper end is driven in a circular motion of frequency f_1 was studied experimentally and numerically. The helix's tension in the experiment increased for f_1 above certain threshold and the structure collapsed at $f_1 \approx 5\text{ Hz}$. Simulation analysis revealed a resonance of the structure at a frequency higher to the one observed in the experiment (around 13 Hz).

1 Introduction

The increase of wind power density with altitude (Archer and Caldeira, 2009) constitutes an important driver for wind technologies. Conventional wind turbines increased notably their size during the last decades to reach higher winds. However, although control strategies were developed to meet efficiency and reliability requirements (Njiri and Soffker, 2016), structural considerations may set an upper limit. Airborne Wind Energy systems (AWES), mainly based on soft kites, rigid-wings, or rotors linked to the ground by tethers, can harvest energy at high altitudes by using the tether tension or onboard wind turbines (Schmehl, 2018; Malz et al., 2022). In Ground-Gen AWE concepts the conversion from mechanical to electrical energy happens on the ground, whereas in Fly-Gen systems such conversion is done on the aircraft (Cherubini et al., 2015). Some of these technologies are in a precommercial state (European Commission, 2018; Blanch et al., 2022). Although it is still unclear which



25 of them will dominate the market among the plethora of existing architectures (van de Kaa and Kamp, 2021), system reliability, operational robustness, safety are crucially important aspects of system development (Salma et al., 2020) together with their performances in realistic vertical wind velocity profiles (Sommerfeld et al., 2019; Schelbergen et al., 2020; Sommerfeld et al., 2023).

30 An interesting subfamily of AWE systems involves concepts based on rotating kites or rotors that use the well-known phenomenon of auto-rotation for harvest wind energy (Rimkus and Das, 2013). An example is a tethered autogyro system with four rotors in a quadrotor configuration that harvests energy and transmits it to the ground via the tether (Mackertich and Das, 2016). *Rotating reel parotors*, which combine rotary ring kites with ground-based rotating reel conversion systems (Benhaiem and Schmehl, 2018) and gyrocopter-type airborne wind turbines (Rancourt et al., 2016; Roberts et al., 2007), have been proposed. Prototypes of AWE systems aimed at the direct transmission of the mechanical torque produced by a set of 35 kites or a flying rotor to a generator on the ground have also been manufactured and tested. The Daisy Stack by Windswept & Interesting Ltd (Read, 2018) and the Rotary AWE (RAWE) machine of SomeAwe (Beaupoil, 2017) belong to this category. These two concepts have in common the use of a light tensegrity structure (Motro, 2003) to transmit the torque to the generator and an auxiliary kite to provide extra lift and fix the elevation angle of the machine.

40 Flight testing activities with the RAWE machine showed that the tensegrity structure exhibits a rich dynamic that involves longitudinal, lateral, and torsional waves. The tensegrity structure has a helix-like shape that acquires a high torsional and bending stiffness when a traction load is applied. Finding the operational limits of the helix is crucial for the reliability of the RAWE machine. According to experimental tests, the structure can collapse if the torque is above certain threshold (Beaupoil, 2022). Numerical simulations can help to predict these operational boundaries but the modeling of the structure represents an 45 important challenge that should balance fidelity and computational cost. Two dynamic models of different complexity have been developed in a previous work for the tensegrity structure of the Daisy Stack (Tulloch et al., 2020, 2023): a simple spring-disc model, and a multi-spring/multi-punctual mass model. The later involves a higher number of degrees of freedom and can capture the variation in axial tension along the length of the structure. Interestingly, two stable equilibrium states were predicted by the numerical simulations when the rotor dynamics was coupled with the spring-disc model (Tulloch et al., 2020). The control problem was also studied by using a model with a small number of degrees of freedom (De Schutter et al., 2018) 50 and the aerodynamic of the rotor was studied with blade-element theory and vortex computations (Pfister and Blondel, 2020).

55 An important property of the tensegrity structures of RAWE machines is that they are slender, i.e. their unstretched length (L_0) and characteristic radius (R_s) satisfy $L_0 \gg R_s$. This work exploits this key feature to model the structure by using Cosserat theory that, due to its versatility, has been used in a very broad range of applications (Ramézani et al., 2011; Riahi and Curran, 2009). In this case, we use Cosserat rod theory to find a set of partial differential equations that govern the dynamic of the central line and its torsional deformation (see Sec. 2). This set of equations are appropriate for investigating in detail the rich dynamic observed in RAWE experiments because it captures the stretching, bending, and twisting of the structure. A finite element method is proposed in Sec. 3 to approximate the partial differential equations by a set of ordinary differential equations. The axial, bending, and torsional stiffness, which naturally appear in the dynamic equations, have been determined experimentally in Sec. 4 for the RAWE machine of SomeAwe. Three scenarios of increasing complexity are studied numerically



60 and experimentally in Sec. 5. Section 6 summarizes the conclusions. The code presented in this work is part of the open-source software LAKSA (Sánchez-Arriaga et al., 2017, 2019).

2 A model for rotary AWE machines

2.1 Kinematics considerations

Figure 1 shows a RAWE machine made of a tensegrity structure (helix) of unstretched length L_0 that transmits the torque generated by a set of blades to a generator on the ground. The slenderness of the tensegrity structure ~~suggests to use~~ some approximations ~~that help~~ to simplify the mathematical analysis. In particular, we ~~just~~ compute the evolution of the position vector of the central line of the helix and an additional angle that orientates the cross-section, which is assumed unshearable. These two variables are called $\mathbf{r}(s, t)$ and $\alpha(s, t)$, with $0 \leq s \leq L_0$ and t ~~the~~ unstretched arc-length and time, respectively. Consequently, the model captures the axial deformation, the bending and the twisting of the helix. An inertial frame of reference 70 \mathcal{S}_E with origin at the generator, plane $x_E - y_E$ spanning the ground, and the z_E -axis pointing downwards is introduced. Therefore, $\mathbf{r}(0, t) = 0$ is the origin of \mathcal{S}_E and $\mathbf{r}(L, t) = \mathbf{r}_T$ is the position vector of the hub of the blades (point T in Fig. 1).

Following Ref. Buckingham (2003), we define at every point of the center line a Frenet frame (\mathcal{S}_F) with axes spanned by the unit vectors $(\mathbf{t}, \mathbf{n}, \mathbf{b})$. For small axial deformations of the helix

$$|\frac{d\mathbf{r}}{ds}| - 1 \ll 1, \quad (1)$$

75 the vectors of the Frenet basis read

$$\mathbf{t} = \mathbf{r}', \quad \mathbf{n} = \frac{\mathbf{r}''}{\kappa}, \quad \mathbf{b} = \mathbf{t} \times \mathbf{n} \quad (2)$$

and the curvature and torsion of the center line are given by

$$\kappa = (\mathbf{r}'' \cdot \mathbf{r}'')^{1/2}, \quad \gamma = \frac{\mathbf{r}' \cdot (\mathbf{r}'' \times \mathbf{r}''')}{\mathbf{r}'' \cdot \mathbf{r}''} \quad (3)$$

where we denoted by the superscript ' the derivative with respect to the unstretched arc-length s . The derivatives of this basis 80 with respect to the arc length are

$$\mathbf{t}' = \boldsymbol{\Omega} \times \mathbf{t}, \quad \mathbf{n}' = \boldsymbol{\Omega} \times \mathbf{n}, \quad \mathbf{b}' = \boldsymbol{\Omega} \times \mathbf{b} \quad (4)$$

where $\boldsymbol{\Omega} = \kappa \mathbf{b} + \gamma \mathbf{t}$ is the Darboux vector.

At every point of the center line we also define a local frame \mathcal{S}_D with director vectors $(\mathbf{d}_1, \mathbf{d}_2, \mathbf{d}_3)$ and origin at the particular point of the center line. The director vector \mathbf{d}_3 points along the tangent vector \mathbf{t} . Vectors \mathbf{d}_1 and \mathbf{d}_2 span the cross section of 85 the helix and are directed along its principal axes of inertia. The director basis is related to the Frenet frame by a rotation of an angle α about the tangent vector \mathbf{t}

$$\begin{pmatrix} \mathbf{d}_1 \\ \mathbf{d}_2 \end{pmatrix} = \begin{pmatrix} \cos \alpha & -\sin \alpha \\ \sin \alpha & \cos \alpha \end{pmatrix} \begin{pmatrix} \mathbf{n} \\ \mathbf{b} \end{pmatrix} \quad (5)$$

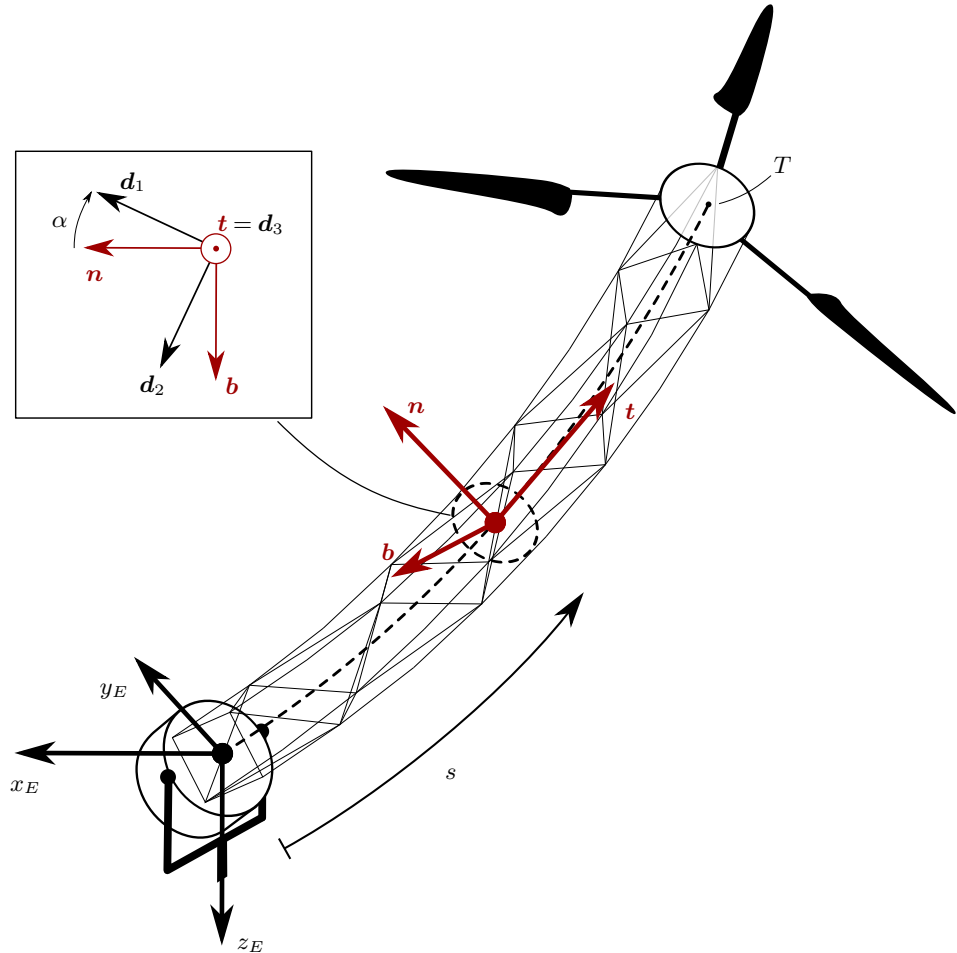


Figure 1. Sketch and frames of reference of the rotary AWE machine.

The derivative of the director basis along the center line is

$$d'_1 = \mathbf{K} \times d_1, \quad d'_2 = \mathbf{K} \times d_2, \quad d'_3 = \mathbf{K} \times d_3 \quad (6)$$

90 where

$$\mathbf{K} = \Omega + \frac{\partial \alpha}{\partial s} d_3 = \kappa \mathbf{b} + \tau \mathbf{t} \quad (7)$$

is the twist vector and it involves the curvature κ and torsion γ of the center line. The scalar

$$\tau \equiv \gamma + \frac{\partial \alpha}{\partial s} \quad (8)$$

95 is the total twist of the principal axes of inertia of the helix about \mathbf{t} . The time evolution of the director vectors is given by an equation analogous to Eq. (6)

$$\dot{d}_1 = \boldsymbol{\omega}_{DE} \times d_1, \quad \dot{d}_2 = \boldsymbol{\omega}_{DE} \times d_2, \quad \dot{d}_3 = \boldsymbol{\omega}_{DE} \times d_3 \quad (9)$$



where the dot denotes time derivative and ω_{DE} is the angular velocity of the local frame with respect to the inertial frame. Vectors ω_{DE} and \mathbf{K} are linked by the constraint

$$\frac{\partial \omega_{DE}}{\partial s} - \frac{\partial \mathbf{K}}{\partial t} = \omega_{DE} \times \mathbf{K}, \quad (10)$$

100 which is found by differentiating Eq. (6) with respect to time and Eq. (9) with respect to the arc length. The angular velocities of frames \mathcal{S}_D and \mathcal{S}_F with respect to \mathcal{S}_E are related by $\omega_{DE} = \omega_{FE} - \dot{\alpha}t$.

2.2 Dynamic model

Momentum and angular momentum equations of the structure with total mass M read (see for instance Ref. Villaggio (2005))

$$\rho A \ddot{\mathbf{r}} = \mathbf{f}' + \rho A g \mathbf{k}_E + \mathbf{F}_A \quad (11)$$

$$105 \quad \rho (I_2 \ddot{\mathbf{d}}_1 \times \mathbf{d}_1 + I_1 \ddot{\mathbf{d}}_2 \times \mathbf{d}_2) = \mathbf{m}' + \mathbf{r}' \times \mathbf{f} \quad (12)$$

where \mathbf{F}_A is the aerodynamic force per unit length, and \mathbf{f} and \mathbf{m} are the internal force and torque, respectively. We also introduced the density $\rho = M/L_0 A$ and the two principal moments of the cross section of area A

$$I_1 = \iint_A x_2^2 dx_1 dx_2, \quad I_2 = \iint_A x_1^2 dx_1 dx_2 \quad (13)$$

Regarding \mathbf{F}_A , we just consider the aerodynamic drag and write

$$110 \quad \mathbf{F}_A = -\frac{1}{2} \rho_0 l_a C_D v_A \mathbf{v}_A, \quad (14)$$

where C_D and ρ_0 are the drag coefficient and the air density. We also defined the aerodynamic velocity ($\mathbf{v}_A = \mathbf{v} - \mathbf{v}_w$), $\mathbf{v} \equiv d\mathbf{r}/dt$, the wind velocity (\mathbf{v}_w), and the characteristic transversal length (l_a), which can be approximated by the sum of the diameters of the bars of the helix. In our analysis we will consider a constant wind velocity vector $\mathbf{v}_w = -v_{w0} \mathbf{i}_E$.

The model is completed by the constituent relations that depend on the elastic properties of the material and on the shape 115 and the dimension of the cross section of the structure. Writing the twist vector as $\mathbf{K} = K_1 \mathbf{d}_1 + K_2 \mathbf{d}_2 + K_3 \mathbf{d}_3$, the internal moment is Love (1892)

$$\mathbf{m} = EI_1 K_1 \mathbf{d}_1 + EI_2 K_2 \mathbf{d}_2 + G J K_3 \mathbf{d}_3 \quad (15)$$

where E is the Young's modulus, G is the rigidity modulus and J is the torsion constant. Hereafter, we will model the structure as a hollow cylinder of radius R_s and thickness h_s . Therefore, we have from Eq. (13)

$$120 \quad I_1 = I_2 = I \equiv \pi R_s^3 h_s, \quad J = 2\pi R_s^3 h_s \quad (16)$$

and, using Eq. (7), Eq. (15) becomes

$$\mathbf{m} = EI \kappa \mathbf{b} + G J \tau \mathbf{t}, \quad (17)$$



The set of equations is simplified if some considerations based on the geometry of the structure and the forces and torques that are expected to act on it are taken into account. We start by assuming that $|\dot{\alpha}| >> |\omega_{FE}|$ and writing $\omega_{DE} \approx -\dot{\alpha}t$. The 125 left hand side of Eq. (12) then becomes

$$\rho \left(I_2 \ddot{\mathbf{d}}_1 \times \mathbf{d}_1 + I_1 \ddot{\mathbf{d}}_2 \times \mathbf{d}_2 \right) = 2\rho I \ddot{\alpha} t, \quad (18)$$

where we used Eq. (9). Regarding the right hand side, we use Eq. (4) and write $\mathbf{f} = T\mathbf{t} + \mathbf{f}_\perp$ with $\mathbf{f}_\perp \cdot \mathbf{t} = 0$ to find

$$\mathbf{m}' + \mathbf{r}' \times \mathbf{f} = GJ\tau' \mathbf{t} + \mathbf{t} \times [\mathbf{f}_\perp - GJ\kappa\tau \mathbf{b} + EI(\kappa \mathbf{n})'] \quad (19)$$

Equation (12) then becomes

$$130 \quad 2\rho I \ddot{\alpha} t = GJ\tau' \mathbf{t} + \mathbf{t} \times [\mathbf{f}_\perp - GJ\kappa\tau \mathbf{b} + EI(\kappa \mathbf{n})']. \quad (20)$$

The components normal to \mathbf{t} of Eq. (20) gives \mathbf{f}_\perp and the total internal force then becomes

$$\begin{aligned} \mathbf{f} &= (T - EI\kappa^2) \mathbf{t} + GJ\kappa\tau \mathbf{b} - EI(\kappa \mathbf{n})' \\ &= (T - EI\kappa^2) \mathbf{r}' + GJ\tau \mathbf{r}' \times \mathbf{r}'' - EI \mathbf{r}''' \end{aligned} \quad (21)$$

where we used Eq (2). For the tension we assume the Hooke's law

$$135 \quad T = EA(|\mathbf{r}'| - 1) \quad (22)$$

This law is consistent with our assumption $(\nu - 1) \ll 1$, which was also used in Eq. (2). For large deformations, the model should be revisited.

After substituting these results in Eqs. (11) and (20), one finds

$$\rho A \ddot{\mathbf{r}} = \{ (T - EI\kappa^2) \mathbf{r}' + GJ\tau (\mathbf{r}' \times \mathbf{r}'') \}' - EI \mathbf{r}''' + \rho Ag \mathbf{k}_E + \mathbf{F}_A \quad (23)$$

$$140 \quad 2\rho I \ddot{\alpha} = GJ(\alpha'' + \gamma') \quad (24)$$

The above set of equations describes the dynamics of the center line of the helix and its torsional deformation. Given appropriate initial and boundary conditions, they can be integrated numerically to find their evolution.

For convenience, we introduce the normalized variables

$$\tilde{t} \equiv \sqrt{\frac{g}{L_0}} t, \quad \tilde{s} \equiv \frac{s}{L_0}, \quad \tilde{\mathbf{r}}(\tilde{s}, \tau) \equiv \frac{\mathbf{r}}{L_0}, \quad \tilde{\mathbf{v}}_A \equiv \frac{\mathbf{v}_A}{\sqrt{gL_0}}, \quad (25)$$

145 parameters

$$\mu \equiv \frac{EI}{MgL_0^2}, \quad \beta \equiv \frac{GJ}{MgL_0^2}, \quad \nu \equiv \frac{\rho_0 l_a L_0^2}{2M} C_D \quad (26)$$

$$\sigma \equiv \frac{EA}{Mg}, \quad \delta \equiv \frac{GJ}{2\rho I g L_0} = \frac{\beta\sigma}{2\mu}, \quad \tilde{v}_{w0} = \frac{v_{w0}}{\sqrt{gL_0}} \quad (27)$$



and normalized forces

$$\tilde{\mathbf{F}}_A(s) \equiv \frac{L_0 \mathbf{F}_A}{Mg} = -\nu \tilde{v}_A \tilde{\mathbf{v}}_A, \quad (28)$$

$$150 \quad \tilde{T}(s) \equiv \frac{T}{Mg} \equiv \sigma(|\tilde{\mathbf{r}}'| - 1). \quad (29)$$

We also changed the notation and the primes ~~denotes now~~ derivative with respect to the normalized arc-length \tilde{s} . The equations of motion become

$$\frac{\partial^2 \tilde{\mathbf{r}}}{\partial \tilde{t}^2} = [\tilde{\mathbf{F}}_{NL} - \tilde{\mathbf{F}}_L]' + \mathbf{k}_E + \tilde{\mathbf{F}}_A \quad (30)$$

$$\frac{\partial^2 \alpha}{\partial \tilde{t}^2} = \delta \tilde{\tau}' \quad (31)$$

155 with

$$\tilde{\mathbf{F}}_{NL} = (\tilde{T} - \mu \tilde{\kappa}^2) \tilde{\mathbf{r}}' + \beta \tilde{\tau} (\tilde{\mathbf{r}}' \times \tilde{\mathbf{r}}''), \quad (32)$$

$$\tilde{\mathbf{F}}_L = \mu \tilde{\mathbf{r}}''', \quad (33)$$

and

$$\tilde{\kappa} = (\tilde{\mathbf{r}}'' \cdot \tilde{\mathbf{r}}'')^{1/2}, \quad \tilde{\gamma} = \frac{\tilde{\mathbf{r}}' \cdot (\tilde{\mathbf{r}}'' \times \tilde{\mathbf{r}}''')}{\tilde{\mathbf{r}}'' \cdot \tilde{\mathbf{r}}''}, \quad \tilde{\tau} \equiv \tilde{\gamma} + \frac{\partial \alpha}{\partial \tilde{s}} \quad (34)$$

160 Regarding the boundary conditions, we do not impose the exact conditions of a real rotary machine, i.e. coupling the dynamics of the structure and the rotor. Such a complete analysis is beyond the scope of this work that is focused on the helix. We use that the position vector of the central line at $\tilde{s} = 0$ coincides with the origin of the inertial system \mathcal{S}_E . At $\tilde{s} = 1$, we also imposed a prescribed position. We then have

$$\tilde{\mathbf{r}}(0, \tilde{t}) = 0, \quad (35)$$

$$165 \quad \tilde{\mathbf{r}}(1, \tilde{t}) = \tilde{\mathbf{r}}_N(\tilde{t}) \quad (36)$$

Additionally, we impose zero curvature at both tips

$$\tilde{\mathbf{r}}''(0, \tilde{t}) = 0, \quad \tilde{\mathbf{r}}''(1, \tilde{t}) = 0 \quad (37)$$

and known torsional torques at $\tilde{s} = 0$ and $\tilde{s} = 1$

$$\tilde{\tau}(0, \tilde{t}) = \frac{\partial \alpha}{\partial \tilde{s}} \Big|_{\tilde{s}=0, \tilde{t}} = m_0(\tilde{t}) \equiv \frac{LM_0(t)}{GJ}, \quad (38)$$

$$170 \quad \tilde{\tau}(1, \tilde{t}) = \frac{\partial \alpha}{\partial \tilde{s}} \Big|_{\tilde{s}=1, \tilde{t}} = m_N(\tilde{t}) \equiv \frac{LM_N(t)}{GJ}, \quad (39)$$

where $M_0(t)$ and $M_N(t)$ are the external torques imposed at the ends of the structure. Equations (38)-(39) involve the use of (3) and (37) in (8). As explained below, the initial conditions depend on the type of analysis.



Since our work does not couple the helix with a rotor, the torque at $\tilde{s} = 1$ is a given function $m_N(\tilde{t})$. Regarding the torque at $\tilde{s} = 0$, we implement the controller

$$175 \quad \dot{m}_0(\tilde{t}) = \dot{m}_N(\tilde{t}) + k_1 [\dot{\alpha}_1(\tilde{t}) - \dot{\alpha}^*] + k_2 \ddot{\alpha}_1(\tilde{t}), \quad (40)$$

where k_1 and k_2 are constant and $\ddot{\alpha}$ is given by the first equation in (62). Such a proportional-derivative controller adjust the torque exerted at the ground to reach a (constant) target angular velocity $\dot{\alpha}^*$ at the first node.

3 A Finite element method

Equations Eqs. (30)-(31) were solved numerically by using a finite element method. We introduce N elements and $N+1$ nodes, $\tilde{r}_j(\tilde{t}) \equiv \tilde{r}(\tilde{s}_j, \tilde{t})$ and $\alpha_j(\tilde{t}) = \alpha(\tilde{s}_j, \tilde{t})$ with $\tilde{s}_j = j/N$, and $j = 0, 1, \dots, N$. For each element between nodes \tilde{r}_j and \tilde{r}_{j+1} , the variables $\tilde{r}(\tilde{s}, \tilde{t})$ and $\alpha(\tilde{s}, \tilde{t})$ are written as Buckham (2003)

$$\tilde{r}(\tilde{s}, \tilde{t}) = \sum_{k=0}^1 \tilde{r}_{j+k}(\tilde{t}) N_k^j(\tilde{s}) + \tilde{r}_{j+k}''(\tilde{t}) H_k^j(\tilde{s}) \quad (41)$$

$$\alpha(\tilde{s}, \tilde{t}) = \sum_{k=0}^1 \alpha_{j+k}(\tilde{t}) N_k^j(\tilde{s}) + \alpha_{j+k}''(\tilde{t}) H_k^j(\tilde{s}) \quad (42)$$

with $\tilde{s}_j \leq \tilde{s} \leq \tilde{s}_{j+1}$. The shape functions are the twisted spline polynomials

$$185 \quad N_0^j(\tilde{s}) = 1 - \xi_j, \quad H_0^j(\tilde{s}) = -\frac{1}{6} (\xi_j^3 - 3\xi_j^2 + 2\xi_j) \quad (43)$$

$$N_1^j(\tilde{s}) = \xi_j, \quad H_1^j(\tilde{s}) = \frac{1}{6} (\xi_j^3 - \xi_j) \quad (44)$$

with

$$\xi_j = \frac{\tilde{s} - \tilde{s}_j}{\tilde{s}_{j+1} - \tilde{s}_j} \quad (45)$$

the local coordinate. One readily verifies that the coefficients $\tilde{r}_j(\tilde{t})$ and $\alpha_j(\tilde{t})$ in Eq. (41) and (42) coincide with the displacements and the rotation angles at the nodes and $\tilde{r}_j''(\tilde{t})$ and $\alpha_j''(\tilde{t})$ with their second derivatives. This choice for the shape function thus gives continuity for $\tilde{r}(\tilde{s}, \tilde{t})$, $\tilde{r}''(\tilde{s}, \tilde{t})$, $\alpha(\tilde{s}, \tilde{t})$ and $\alpha''(\tilde{s}, \tilde{t})$. If we now impose that the first derivative be continuous across the elements, we find the following relation between $\tilde{r}_j''(\tilde{t})$ and $\tilde{r}_j(\tilde{t})$ Press et al. (1992)

$$B_r \begin{pmatrix} \tilde{r}_1'' \\ \tilde{r}_2'' \\ \tilde{r}_3'' \\ \dots \\ \tilde{r}_{N-1}'' \end{pmatrix} = C_r \begin{pmatrix} \tilde{r}_0 \\ \tilde{r}_1 \\ \tilde{r}_2 \\ \dots \\ \tilde{r}_N \end{pmatrix} \quad (46)$$



with

$$195 \quad \mathbf{B}_r = \begin{pmatrix} 2\mathbf{I}/3 & \mathbf{I}/6 & 0 & 0 & \dots & 0 \\ \mathbf{I}/6 & 2\mathbf{I}/3 & \mathbf{I}/6 & 0 & \dots & 0 \\ 0 & \mathbf{I}/6 & 2\mathbf{I}/3 & \mathbf{I}/6 & \dots & 0 \\ 0 & \dots & \dots & \dots & \dots & \dots \\ 0 & \dots & \dots & \dots & \mathbf{I}/6 & 2\mathbf{I}/3 \end{pmatrix}_{3(N-1) \times 3(N-1)} \quad (47)$$

$$C_r = \begin{pmatrix} \mathbf{I} & -2\mathbf{I} & \mathbf{I} & 0 & \dots & 0 \\ 0 & \mathbf{I} & -2\mathbf{I} & \mathbf{I} & \dots & 0 \\ 0 & 0 & \mathbf{I} & -2\mathbf{I} & \mathbf{I} & 0 \\ 0 & \dots & \dots & \dots & \dots & \dots \\ 0 & \dots & \dots & \dots & \dots & \dots \\ 0 & 0 & \dots & \mathbf{I} & -2\mathbf{I} & \mathbf{I} \end{pmatrix}_{3(N-1) \times 3(N+1)} \quad (48)$$

and we used the boundary conditions $\mathbf{r}''(0, \tilde{t}) = \mathbf{r}''(1, \tilde{t}) = 0$. For α , the continuity condition for α' across the elements gives

$$\mathbf{B}_\alpha \begin{pmatrix} \alpha_0'' \\ \alpha_1'' \\ \dots \\ \alpha_{N-1}'' \\ \alpha_N'' \end{pmatrix} = \mathbf{C}_\alpha \begin{pmatrix} \alpha_0 \\ \alpha_1 \\ 0 \\ \alpha_{N-1} \\ \dots \\ \alpha_N \end{pmatrix} + \begin{pmatrix} -m_0 \\ 0 \\ \dots \\ 0 \\ m_N \end{pmatrix} \quad (49)$$

with

$$200 \quad \mathbf{B}_\alpha = \begin{pmatrix} 1/3 & 1/6 & 0 & 0 & \dots & 0 \\ 1/6 & 2/3 & 1/6 & 0 & \dots & 0 \\ 0 & 1/6 & 2/3 & 1/6 & \dots & 0 \\ 0 & \dots & \dots & \dots & \dots & \dots \\ 0 & \dots & \dots & 1/6 & 1/3 & 1/6 \\ 0 & \dots & \dots & \dots & 1/6 & 1/3 \end{pmatrix}_{(N+1) \times (N+1)} \quad (50)$$

$$C_\alpha = \begin{pmatrix} -1 & 1 & 0 & 0 & \dots & 0 \\ 1 & -2 & 1 & 0 & \dots & 0 \\ 0 & 1 & -2 & 1 & 0 & 0 \\ \dots & \dots & \dots & \dots & \dots & \dots \\ 0 & \dots & \dots & 1 & -2 & 1 \\ 0 & \dots & \dots & 0 & 1 & -1 \end{pmatrix}_{(N+1) \times (N+1)} \quad (51)$$



where we used the boundary conditions $\alpha'(0, \tilde{t}) = m_0$ and $\alpha'(1, \tilde{t}) = m_N$. Equations (41)-(42) for all the elements, together with relations (46)-(49) and the boundary condition Eqs. (35)-(36), allows to write the variables as

$$\tilde{\mathbf{r}}(\tilde{s}, \tilde{t}) = \sum_{j=1}^{N-1} \tilde{\mathbf{r}}_j(\tilde{t}) \phi_j(\tilde{s}) + \tilde{\mathbf{r}}_N(\tilde{t}) \phi_N(\tilde{s}) \quad (52)$$

$$205 \quad \alpha(\tilde{s}, \tilde{t}) = \sum_{j=0}^N \alpha_j(\tilde{t}) \varphi_j(\tilde{s}) + m(\tilde{s}, \tilde{t}) \quad (53)$$

where ϕ_i and φ_i are \mathcal{C}^2 continuous functions and the function $m(\tilde{s}, \tilde{t})$ just involves the boundary conditions (m_0 and m_N) and the shape functions. One readily checks that $\phi_i(0) = 0$ for $i = 1 \dots N$, $\phi_N(1) = 1$, and $\phi_i(1) = 0$ for $i = 0, \dots N-1$.

Following a Galerkin method, we write Eqs. (30)-(31) in the weak form. We multiply Eq. (30) by ϕ_i with $i = 1 \dots N-1$, and Eq. (31) by φ_i with $i = 0 \dots N$, and integrate between $\tilde{s} = 0$ and $\tilde{s} = 1$ to find

$$210 \quad \sum_{j=1}^{N-1} P_{ij}^{(0)} \ddot{\mathbf{r}}_j = \mathbf{a}_{iN} + \mathbf{p}_i^{(0)} + \int_0^1 \left[(\tilde{\mathbf{F}}_{NL} - \tilde{\mathbf{F}}_L)' + \tilde{\mathbf{F}}_A \right] \phi_i d\tilde{s}, \quad i = 1 \dots N-1 \quad (54)$$

$$\sum_{j=0}^N Q_{ij}^{(0)} \ddot{\alpha}_j = \ddot{m}_i^0 + \delta \int_0^1 \tilde{\tau}' \varphi_i(\tilde{s}) d\tilde{s}, \quad i = 0 \dots N \quad (55)$$

where we introduced the matrices and the vectors

$$P_{ij}^{(0)} = \int_0^1 \phi_j(\tilde{s}) \phi_i(\tilde{s}) d\tilde{s} \quad (56)$$

$$\mathbf{a}_{iN} = - \ddot{\mathbf{r}}_N \int_0^1 \phi_i(\tilde{s}) \phi_N(\tilde{s}) d\tilde{s} \quad (57)$$

$$215 \quad \mathbf{p}_i^{(0)} = \mathbf{k}_E \int_0^1 \phi_i(\tilde{s}) d\tilde{s} \quad (58)$$

$$Q_{ij}^{(0)} = \int_0^1 \varphi_j(\tilde{s}) \varphi_i(\tilde{s}) d\tilde{s} \quad (59)$$

$$\ddot{m}_i^0 = - \int_0^1 \ddot{m}(\tilde{s}, \tilde{t}) \varphi_i(\tilde{s}) d\tilde{s} \quad (60)$$



Integrations by parts of Eq. (54) and (55) yield

$$\begin{aligned}
 \sum_{j=1}^{N-1} P_{ij}^{(0)} \ddot{\tilde{r}}_j &= \mathbf{a}_{iN} + \mathbf{p}_i^{(0)} + \int_0^1 \tilde{\mathbf{F}}_A \phi_i d\tilde{s} - \int_0^1 \left(\tilde{\mathbf{F}}_{NL} - \tilde{\mathbf{F}}_L \right) \phi'_i d\tilde{s} \\
 &= \mathbf{a}_{iN} + \mathbf{p}_i^{(0)} - \mu \sum_{j=1}^N P_{ij}^{(4)} \tilde{r}_j + \int_0^1 \left(\tilde{\mathbf{F}}_A \phi_i - \tilde{\mathbf{F}}_{NL} \phi'_i \right) d\tilde{s}, \quad i = 1 \dots N-1
 \end{aligned} \tag{61}$$

$$\sum_{j=0}^N Q_{ij}^{(0)} \ddot{\alpha}_j = \ddot{m}_i^0 + \delta \left\{ [\tilde{\tau} \varphi_i]_0^1 - \sum_{j=0}^N Q_{ij}^1 \alpha_j - \int_0^1 \left(\tilde{\gamma} + \frac{\partial m}{\partial \tilde{s}} \right) \varphi'_i(\tilde{s}) d\tilde{s} \right\}, \quad i = 0 \dots N \tag{62}$$

where we used that $\phi_i(0) = \phi_i(1) = 0$ for $i = 1 \dots N-1$, Eq. (37), and defined

$$Q_{ij}^{(1)} = \int_0^1 \varphi'_j(\tilde{s}) \varphi'_i(\tilde{s}) d\tilde{s} \tag{63}$$

$$P_{ij}^{(4)} = \int_0^1 \phi''_j(\tilde{s}) \phi''_i(\tilde{s}) d\tilde{s} \tag{64}$$

225 Since i runs from 1 to $N-1$ in Eq. (61), and from 0 to N in Eq (62), there are a total of $3(N-1) + N + 1 = 4N-2$ equations for the $4N-2$ unknowns, which are $\tilde{r}_j(\tilde{t})$ with $j = 1 \dots N-1$ and $\alpha_j(\tilde{t})$ with $j = 0 \dots N$.

After constructing the vector

$$\mathbf{q}_s = [\tilde{r}_1 \quad \tilde{r}_2 \dots \tilde{r}_{N-1} \quad \alpha_0 \dots \alpha_N] \tag{65}$$

and the stater vector

$$\mathbf{x}_s = [\mathbf{q}_s \quad \dot{\mathbf{q}}_s \quad m_0], \tag{66}$$

we find the following set of first order ordinary differential equations

$$\bar{\mathbf{M}} \dot{\mathbf{x}}_s = \mathbf{g}(\mathbf{x}_s), \quad \text{or,} \quad \dot{\mathbf{x}}_s = \mathbf{f}(\mathbf{x}_s) \equiv \bar{\mathbf{M}}^{-1} \mathbf{g}(\mathbf{x}_s). \tag{67}$$

The explicit form of matrix $\bar{\mathbf{M}}$ and the vector field \mathbf{g} can be found from Eqs. (61), (62) and (40).

Several tests were carried out to verify the correct implementation of Eq. (67). For instance, to test the correct implementation 235 of functions ϕ_j and φ_j , and matrices \mathbf{B}_r , \mathbf{C}_r , etc, some analytical functions satisfying the boundary conditions were proposed for \tilde{r} and $\tilde{\alpha}$. The derivatives $d\tilde{r}/d\tilde{s}$, $d^2\tilde{r}/d\tilde{s}^2$, $d^3\tilde{r}/d\tilde{s}^3$, $d\alpha/ds$, and $d^2\alpha/ds^2$ were computed analytically and also by using the finite element approach. It was verified that both results converge as the number of elements increases. The analysis of Sec. 5.1, where a stationary solution is found with an alternative numerical method, constitute another test of the correct implementation of the finite element method.



240 4 Experimental characterization of the structure

Three laboratory tests were carried out to find the values of EA , EI , and GJ for the tensegrity structure. As shown in the three panels of Fig. 2, a segment of the helix with length equal to $L_0 = 6.76\text{m}$ was clamped on a wall. As explained below, different types of loads were applied to determine the axial, bending, and torsional stiffness. For all the tests, a tension force T_e was applied to the structure and its values were taken in the order of around 200 N, which is the nominal tension during the regular 245 operation of the RAWE machine. In cases (a) and (c) in Fig. 2, i.e. the axial and torsion tests, such axial force was applied by using a tension belt. In the bending experiment [case (b)], where there is a lateral displacement, a pulley and a ballast mass were used and the position of the pulley was adjusted to apply the force normal to the displacement. Panel (d) in Fig. 2 displays the helix configuration during the axial test and the tension belt.

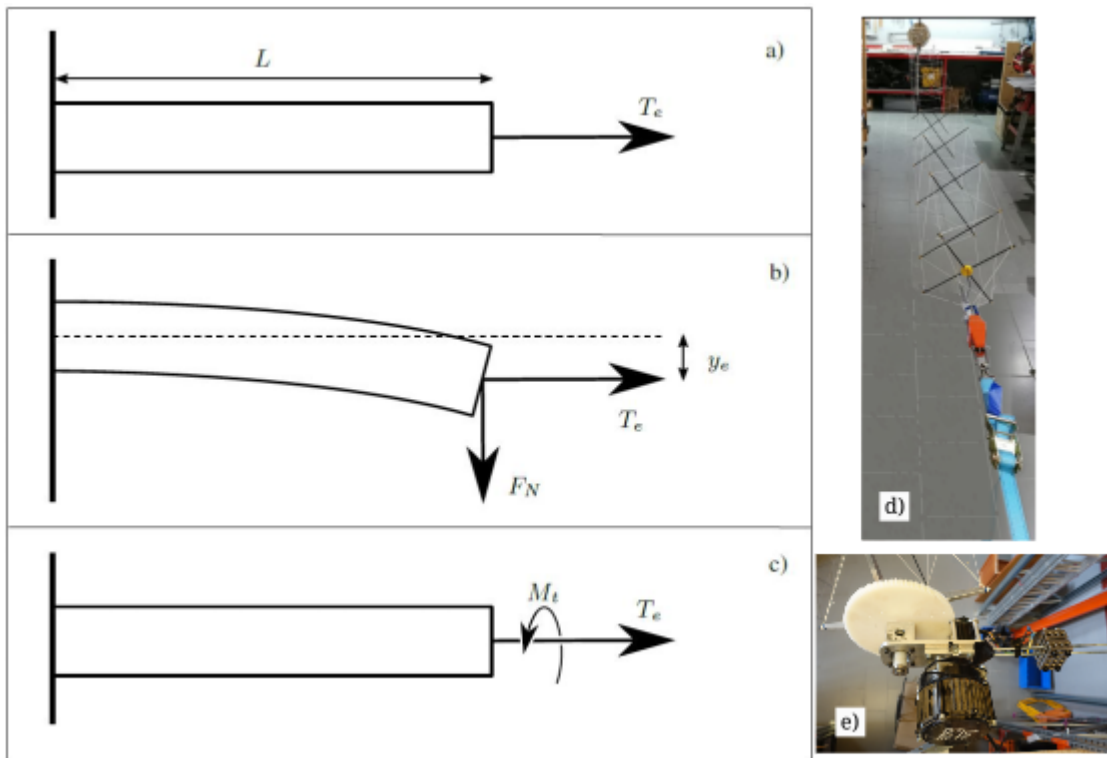


Figure 2. Panels (a)-(c) show the sketches of the axial, bending and torsion tests. Panels (d) and (e) displays the helix in the axial test and the motorized eccentric arm explained in Sec. 5.3.

As shown in the top panel of Fig. 2, the product EA was found by applying an axial force T_e and measuring the resulting 250 length of the structure L . The axial force was varied by just increasing the mass of the ballast. For a linear material, the relation between the axial force and the length of the structure is

$$T_e = EA \times \frac{L - L_0}{L_0} \quad (68)$$



As expected, the experimental values of the strain are proportional to the applied force (see Fig. 3). The slope obtained with a linear regression is $EA = 3.64 \times 10^4$ N.

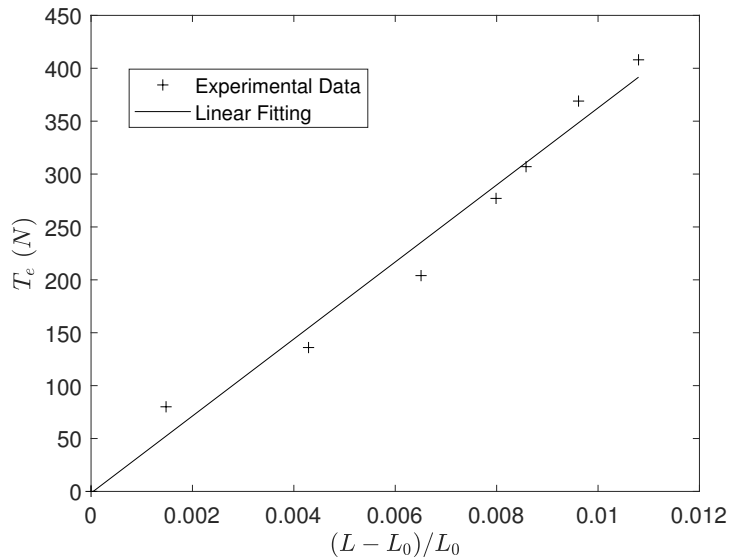


Figure 3. Experimental results of the axial test.

255 A classical bending test was carried out to determine the product EI of the helix. As shown in the middle panel of Fig. 2, a normal force of value F_N was applied at the free end of the structure and the vertical displacement y_e was measured. Since the theoretical relation between both magnitudes is

$$F_N = EI \times \frac{3y_e}{L_0^3}, \quad (69)$$

260 measuring the pairs (F_N, y_e) and making a linear regression to the experimental data gives the product EI . However, the bending stiffness of the tensegrity structure depends on the internal tension force. For this reason, the experiment was carried out for three different ballast masses, which yielded the tension forces $T_e = 90, 181$, and 259 N. As shown in Fig. 4, for each value of the tension, the helix has a different bending stiffness (slope of the linear regression in the F_N versus $3y_e/L_0^3$ plane). The inset in Fig. 4 shows that the relation between the product EI and the tension is also linear and follow the law

$$EI \text{ (Nm}^2\text{)} = 52.4 \times T_e \text{ (N)} + 2290 \quad (70)$$

265 As expected, the higher the tension, the higher the bending stiffness of the tensegrity structure.

Difficulties were found for the experimental determination of the torsional stiffness. As shown in the bottom panel of Fig.

1 the helical structure was tightened with the ballast mass to induce a tension force T_{e0} for zero torsion angle ($\alpha = 0$). A torsion torque M_t was then applied at the free end of the structure until the torsion angle took certain value α . The tension force T_e was then measured with the hanging scale and it was found that it was higher than the one for zero torque, $T_e > T_{e0}$.

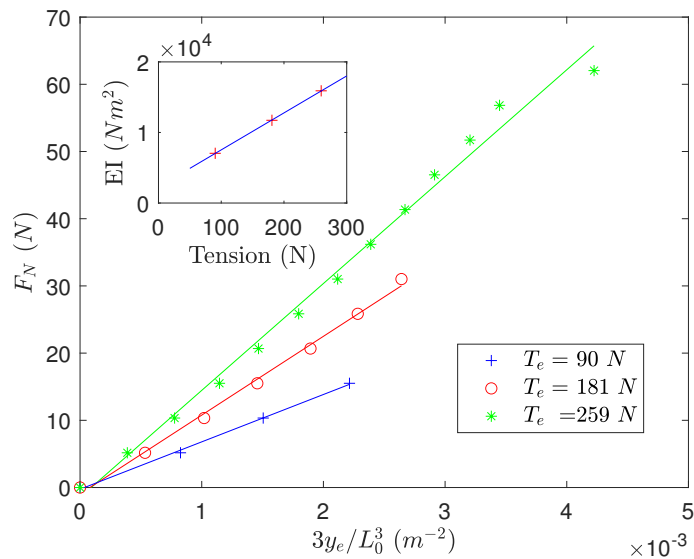


Figure 4. Experimental results of the bending test.

270 Measurements of M_t , α , and T_e were taken by first increasing M_t sequentially and with an increment of the torsion angle around $\Delta\alpha = 10^\circ$. After reaching a maximum torsion angle of about 50° , M_t was lowered to produce decrements in the torsion angle of $\Delta\alpha = -10^\circ$ until $\alpha = 0$ was reached. Four complete cycles raising and lowering the torsional torque were completed and measurements for the three variables (M_t , α , and T_e) were taken. The maximum value of M_t in the experiment was around 25 Nm, which is consistent with the torque measured during the real operation of the RAWE machine.

275 In principle, a simple model for the relation between the torsion torque and angle is

$$M_t = GJ \times \frac{\alpha}{L_0} \quad (71)$$

However, the experiment revealed that the behavior of the helix is not so simple. As seen in Fig. 5, the ratio $M_t L_0 / \alpha$, which may coincide with GJ according to Eq. (71), versus the tension force T_e present hysteresis. For the three tests covering a tension range between 180 and 240 N, the repeatability of the measurements is satisfactory but it is clear that the ratio $M_t L_0 / \alpha$ cannot be parametrized by the tension force T_e alone. In a fourth test, the torsional behavior of the structure was explored at an even larger tension values and the amplitude of the hysteresis cycle was similar. These results indicate that the value of the torsional rigidity does not only depend on the instantaneous values of the torsion angle and internal tension but also on the history of the helix. Such a feature may be due to the peculiar construction of the tensegrity helix, which involves bars under compression, tethers and knots. The unavoidable friction in the experimental setup may also play a role. For this reason, we decided in later 285 analysis to set a nominal value for GJ of 140 Nm^2 , which is consistent with the experimental results of Fig. 5 for $T_e = 200 \text{ N}$.

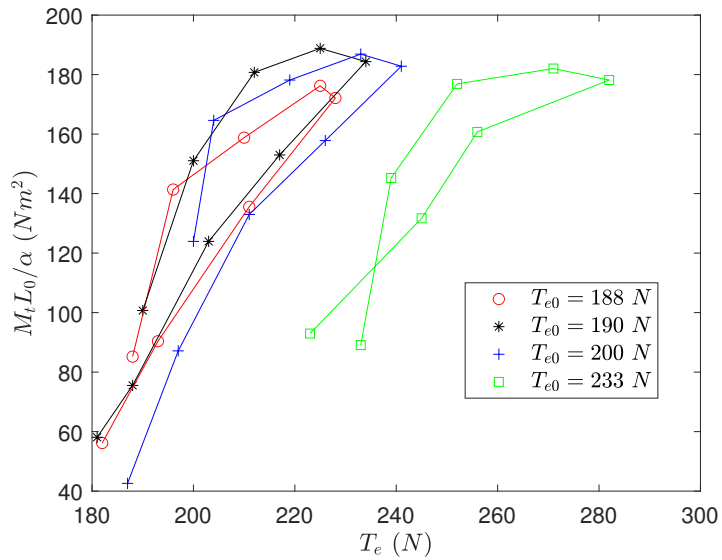


Figure 5. Experimental results of the torsion test.

5 Dynamic of the helix: numerical and experimental results

This section studies three different dynamic scenarios of the helix. For all of them we used the parameters shown in Table 1.

Table 1. Common parameters used in the analysis.

Symbol	Value	Symbol	Value
g	9.81 m/s^2	ρ_0	1.225 kg/m^3
R	0.19 m	l_a	0.012 m
EA	$3.64 \cdot 10^4 \text{ N}$	GJ	140 Nm^2
C_D	1		

5.1 Stationary solutions with fixed ends

290 We consider a helix with the properties of Table 1 and 2, which correspond to the characteristic of the structure of the RAWE machine of SomeAwe. Since its nominal tension during regular operation is around 200 N, we set the elongation of the initial condition as $\epsilon_0 = 200N/EA$ and computed EI by using Eq. (70) with $T_e = 200$ N. The analysis focuses on stationary solutions of Sys. (67) with the boundary conditions given by Eqs. (35)-(36) and

$$\tilde{\mathbf{r}}_N(\tilde{t}) \equiv -(1 + \epsilon_0)(\cos \Gamma_0 \mathbf{i}_E + \sin \Gamma_0 \mathbf{k}_E) \quad (72)$$



Table 2. Parameters used in the analysis of solutions with fixed ends.

Symbol	Value	Symbol	Value
ϵ_0	0.0055	Γ_0	45°
L_0	16.12 m	M	0.51 kg
EI	$1.28 \times 10^4 \text{ Nm}^2$	v_{w0}	10 m/s

295 where Γ_0 is the elevation angle of the helix and ϵ_0 is related to its elongation. We restrict the analysis to solutions of the type $\tilde{r} = x\mathbf{i}_E + z\mathbf{k}_E$ and $\alpha(\tilde{s}, \tilde{t}) = 0$ with $k_1 = k_2 = m_0 = m_N = 0$. Since the proposed solution is contained in the $x_E - z_E$ plane and no torque is applied at the ends of the helix, the torsion vanishes ($\tau(\tilde{s}) = 0$) and Eq. (31) is automatically fulfilled. Regarding Eq. (30), and after using ($\ddot{\tilde{r}} = \dot{\tilde{r}} = 0$), it becomes the following set of ordinary differential equations

$$\frac{d}{d\tilde{s}} \begin{pmatrix} x \\ z \\ x_s \\ z_s \\ x_{ss} \\ z_{ss} \\ x_{sss} \\ z_{sss} \end{pmatrix} = \begin{pmatrix} x_s \\ z_s \\ x_{ss} \\ z_{ss} \\ x_{sss} \\ z_{sss} \\ \left[f_s x_s + (\tilde{T} - \mu \kappa^2) x_{ss} - \nu \tilde{v}_{w0}^2 \right] / \mu \\ \left[f_s z_s + (\tilde{T} - \mu \kappa^2) z_{ss} + 1 \right] / \mu \end{pmatrix} \quad (73)$$

300 with $\kappa^2 = x_{ss}^2 + z_{ss}^2$, $\tilde{T} = \sigma \left(\sqrt{x_s^2 + z_s^2} - 1 \right)$ and

$$f_s = \frac{\sigma}{\sqrt{x_s^2 + z_s^2}} (x_s x_{ss} + z_s z_{ss}) - 2\mu (x_{ss} x_{sss} + z_{ss} z_{sss}) \quad (74)$$

The solution of Sys. (73) compatible with the boundary conditions (35)-(36) was found by using a shooting method. The equations were integrated numerically with a Runge-Kutta method and the state at $s = 0$ given by $(0, 0, x_{s0}, z_{s0}, 0, 0, x_{sss0}, z_{sss0})$. Constants x_{s0} , z_{s0} , x_{sss0} and z_{sss0} were varied with a shooting method until the conditions $x(1) = -(1 + \epsilon_0) \cos \Gamma_0$, $z(1) = -(1 + \epsilon_0) \sin \Gamma_0$, $x_{ss}(1) = z_{ss}(1) = 0$ were satisfied. Once the solution was found, we constructed from it the state vector \mathbf{x}_s of Eq. (66). Its substitution in the right hand side of Eq. (67) revealed that it is indeed a stationary solution because we found $|\mathbf{g}(\mathbf{x}_s)| \approx 0$. The larger the number of finite elements, the lower the value of $|\mathbf{g}(\mathbf{x}_s^*)|$. This result constitutes an important test about the correct implementation of the finite element method because \mathbf{x}_s was found with an alternative numerical algorithm (an integration of the equations with a Runge-Kutta method).

310 The linear stability of the stationary solution was then investigated in the framework of Eq. (67) and setting $N = 2$. Using the vector \mathbf{x}_s obtained with the shooting algorithm as initial guess, we found the state vector satisfying the condition $\mathbf{f}(\mathbf{x}_s^*) = 0$ in Eq. (67) with a Newton-Raphson method. Afterwards, the Jacobian matrix of flow \mathbf{f} at \mathbf{x}_s^* was computed as well as its eigenvalues. As shown in Table 3, the stationary solution is stable because the eigenvalues are pure imaginary numbers or



Table 3. Stability results of the stationary solution. $N = 2$.

Eigenvalues λ	Dominant components	Mode	Period
			(s)
$-2.23 \pm 271.4i$	\dot{x}_1, \dot{z}_1	Longitudinal	0.03
$-2.23 \pm 37i$	\dot{x}_1, \dot{z}_1	Lateral	0.21
$-1.48 \pm 37i$	\dot{y}_1	Lateral	0.21
$\pm 40i$	$\dot{\alpha}_0, \dot{\alpha}_1, \dot{\alpha}_2$	Torsional	0.20
$\pm 20i$	$\dot{\alpha}_0, \dot{\alpha}_2$	Torsional	0.40
$\approx 0 \pm 0i$	$\alpha_0, \alpha_1, \alpha_2$	Torsional	N/A

complex number with negative real part. There are two longitudinal modes where the dominant components of the eigenvectors 315 are \dot{x}_1 and \dot{z}_1 . The first of them has a short period (fast mode), which can be approximated by $T_{Long} \approx 2L_0/\sqrt{E/\rho}$ that is valid for thin and elastic rods of Youngs modulus E and density ρ . In our case it reads $T_{Long} \approx 2\sqrt{ML_0/EA} \approx 0.03$ s and match with the first mode in Table (3). There is also a lateral mode dominated by displacements contained in the $x_E - z_E$ plane. The period of this mode is well described by the one of a string of linear density ρ_L , length L_0 , tension T , and fixed 320 tips. The n-th harmonic vibration has wavelength $\lambda_n = 2L_0/n$ and velocity $\sqrt{T/\rho_L}$. The period for $n = 2$ in our case reads $T_{Lat} \approx \sqrt{ML_0/EA\epsilon_0} \approx 0.20$ s, where we used that the tension is in the order of $EA\epsilon_0$. Regarding the torsional wave, its velocity is $\sim \sqrt{\delta g L_0}$ and the wavelength $\sim 2L_0$. The period then reads $T_{Tor} \approx 2\sqrt{L_0/\delta g} \approx 0.4$ s. The last two modes in Table 3 has zero eigenvalues and correspond to free rotations as a rigid body of the full structure around its mean line.

5.2 Nominal operation of a RAWE machine with fixed ends

We now investigate the dynamic response of the helix when the torque at the upper end varies as

$$325 \quad m_N(\tilde{t}) = m_{N0} [1 - \exp(-\tilde{t}/\tilde{t}_0)] \quad (75)$$

with $m_{N0} = 2.88$ and $\tilde{t}_0 = 2$, which correspond to 25 Nm and 2.6 s. For the controller in Eq. (40), we used $k_1 = k_2 = 0.5$ and a target angular velocity of 120 rpm, which is the nominal value for the operation of the RAWE machine. Both ends of the structure are fixed according to the boundary conditions (35)-(36) and Eq. (72). The initial condition of the simulation is the stationary solution explained in Sec. 5.1. System (67) was integrated numerically with a Runge-Kutta algorithm and for $N = 2$. 330 Since the torques at the ends of the helix depend on time, the term \tilde{m}_i^0 in Eq. (62) involve the third derivative of α at $s = 0$. For its evaluation at every time step during the numerical integration, we used backwards finite difference approximations.

Panel (a) in Fig. 6 shows the evolution of $\dot{\alpha}$ for the three nodes of the structure (dotted, dashed and solid lines) in the simulation. The controller successfully adjusted the torque on the ground [panel (c)] to make the structure rotate at the target angular velocity, which is 120 rpm. As shown in panel (b), the tension is almost constant throughout the helix and equal to 335 around 200 N. The velocity of the nodes (not shown) tends to zero and there is no lateral displacement. Therefore, the long-term state of the helix has its central line inside the $x_E - z_E$ plane in a stationary condition and the angles α for all the nodes rotate



at a constant rate. The conclusions of this paragraph have been corroborated by running simulations with a higher number of elements ($N = 3$ and $N = 5$) and faster raising time of the torque at the upper end ($\tilde{t}_0 = 0.5$ and $\tilde{t}_0 = 1$).

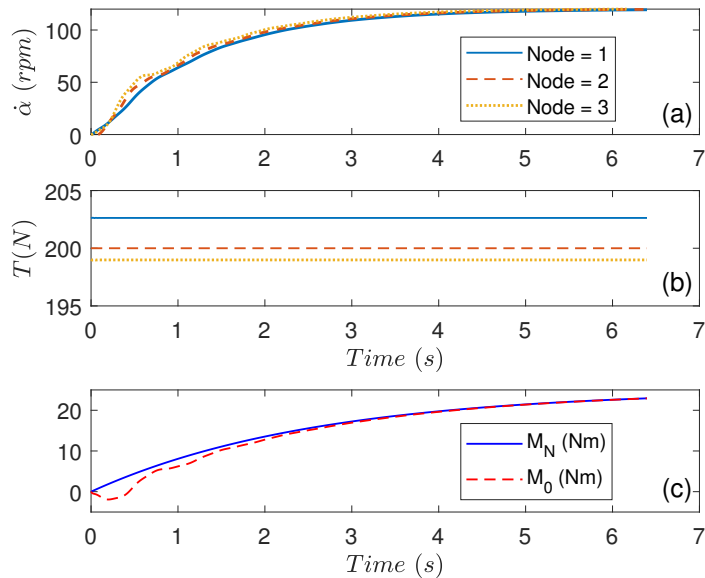


Figure 6. Panels (a), (b), and (c) show the evolution of $\dot{\alpha}$ at the nodes and the target angular velocity (thick solid line), the torque at the ground, and the tensions at the nodes, respectively. The ends of the structure are fixed.

5.3 Dynamic of the RAWE machine with a mobile end

340 The real operation of a RAWE machine is more complex than the scenario described in Sec. 5.2 because the upper end point is mobile. Although an auxiliary kite provides additional lift and helps to anchor it, the motion of the rotor and wind fluctuations naturally drive a motion for the upper end of the structure. This mechanism injects energy into the helix and, as shown below, its dynamics depend heavily on the characteristic frequency of the forcing. Insight into the behavior of the RAWE machine can be obtained by using the model of this work, and still avoiding the coupling with a rotor, by considering the following

345 boundary condition for the upper end

$$\begin{aligned}\tilde{\mathbf{r}}(1, \tilde{t}) = & -[(1 + \epsilon_0) \cos \Gamma_0 + r_1 \sin \Gamma_0 \sin \omega_1 \tilde{t}] \mathbf{i}_E + r_1 \cos \omega_1 \tilde{t} \mathbf{j}_E \\ & - [(1 + \epsilon_0) \sin \Gamma_0 - r_1 \cos \Gamma_0 \sin \omega_1 \tilde{t}] \mathbf{k}_E,\end{aligned}\quad (76)$$

It corresponds to a circular motion of the upper point of the structure with a radius and a frequency of $R_1 = r_1 L_0$ and $f_1 = (\omega_1/2\pi) \sqrt{g/L_0}$, respectively. Its effect on the dynamics of the structure has been studied experimentally and numerically.

350 The experiment, which was carried out inside the laboratory, used a structure with the characteristics of Tables 1 and 4. Although similar to the one considered in Sec. 5.2, we used a structure with a shorter length and lower mass due to space constraints in the laboratory. The nominal tension was also lowered to 80 N and, according to Fig. 4 and Eq. (70), the bending



Table 4. Parameters used in the analysis of solutions with a mobile end.

Symbol	Value	Symbol	Value
ϵ_0	0.002	Γ_0	25°
L_0	7.9 m	M	0.25 kg
EI	4381Nm ²	v_{w0}	0m/s
$d\alpha/dt ^*$	75rpm	M_N	25Nm
k_1	0.5	k_2	0.5
R_1	0.1 m		

stiffness is also lower ($EI = 6483 \text{ Nm}^2$). The nominal tension was adjusted by imposing the adequate distance between the tips of the structure. For this test, the torque was applied into the helix at the ground by a motor that was operated at a steady 355 angular velocity. To impose the circular periodic motion given by Eq. (76), the helix's upper end point was attached to an eccentric arm that was powered with a second motor [see panel (e) in Fig. 2]. A radius of $R_1 = 0.1 \text{ m}$ was used and the frequency f_1 was varied. An electromagnetic brake countered the torque on the eccentric arm. This is opposite of how the system operates in the generation mode of a RAWE machine, where the torque is generated by the rotor and countered by the generator on the ground. Nonetheless, the resulting torque in the helix during the experiment was the same than in a normal 360 operation and this experimental configuration avoided the need for having another motor with its power supply on the arm. Regarding diagnostics, the axial tension on the helix was measured with load cells on the attachment points at the ground.

As shown in Fig. 7, the frequency f_1 of the eccentric arm was increased in multiple steps and the total tension on the structure was measured with load cells. The lateral displacement of the helix was also monitored by using multiple cameras. The experimental data revealed that the tension oscillated at a frequency close to the driving frequency. The oscillations are 365 regular for low frequencies and irregular for a driving frequency close to 5 Hz. It was also observed in the experiment that the amplitude of the oscillations, i.e. the lateral displacement of the central point of the structure, increased with the driving frequency. When the driving frequency reached 5 Hz, the structure collapsed because multiple tethers ripped and the experiment was stopped. Interestingly, and as shown in Fig. 7, changing the forcing frequency from 0.7 Hz to 2.1 Hz did not result into an enhancement of the tension. Only when the frequency was increased up to 3.5 Hz and beyond, higher values were measured by 370 the load cells. According to this experimental results and the simulation results presented below, we conclude that the periodic forcing of the upper end induced a resonance in the structure. The irregular oscillations observed at high frequencies are a signature of the nonlinearities excited by the high values of the tension. They reached values equal to three times the nominal tension before the helix collapsed.

The same scenario was also studied by using the simulator. Besides the parameters of Tables 1 and 4, we imposed the 375 boundary condition given in Eq. (76) and set $N = 2$. We started the analysis at a very low forcing frequency and, for the initial condition, we used the procedure explained in Sec. 5.1. System (67) was then integrated numerically until the helix exhibited regular oscillations. The output tension at $s = 0$ was then post-processed to identify its maxima (T_{max}) in the long term (once

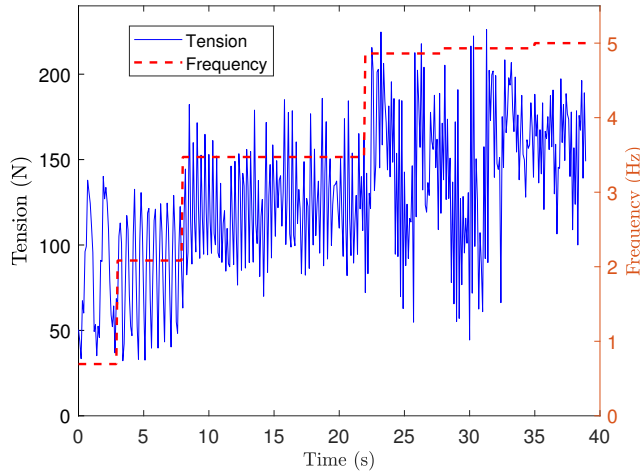


Figure 7. Evolution of the tension (left) and the forcing frequency f_1 (right) in the experiment with a mobile upper end.

the transient phase died out). Afterwards, the value of f_1 was increased and the full process was repeated but now using as initial condition the state of the helix at the end of the previous simulation.

380 The result of the analysis is the bifurcation diagram with T_{max} versus f_1 shown in Fig. 8. Interestingly, it brings out the strengths and weakness of the numerical tool. Regarding the former, the simulator predicts a resonance of the structure similar to the one observed in the experimental data. However, the maximum tension in the simulator raises for driving frequencies above around 9 Hz, whereas in the experiment an enhancement of the tension was detected for lower frequencies (above 3.5 Hz). The inset of Fig. 8 shows the evolution of the tension at $s = 0$ for $f_1 = 10$ Hz in the long term (after the transient has 385 died out). Similarly to the experimental results obtained for low frequencies, the tension oscillates regularly and at a frequency close to f_1 . However, unlike the experimental data, the amplitude of the oscillations in the tension are small (a few newtons), whereas in the experiment they were in the order of tens of newtons.

390 Therefore, we conclude that the numerical tool is able to capture correctly some interesting phenomena and it can be used to predict them qualitatively. However, if the interest is in getting quantitative values, then it should be used carefully. This conclusion is reasonable because the simulator relies on a set of simplifying hypotheses and also needs to be fed with inputs that have certain level of uncertainty. As shown by the results of the experimental characterization of the structure in Sec. 4, the bending and torsional stiffness of the tensegrity structure are difficult to model. They depend on the tension and, in the case of torsional stiffness, it presents hysteresis. Another important topic is the modelling of the damping in the system, which 395 could be improved in future work. The aerodynamic drag, already considered in the model, dissipates energy but there are other mechanisms that may also be included. An example is the friction between elements of the tensegrity structure, which can affect the response of the system shown in Fig. 8. Consequently, the predictive capability of simulations is limited. Nonetheless, each simulation for a given f_1 has a relatively low computational cost (around 1 minute). This opens the possibility to make



analysis varying the physical parameters that are difficult to estimate and tune the simulator for reproducing the experimental results quantitatively.

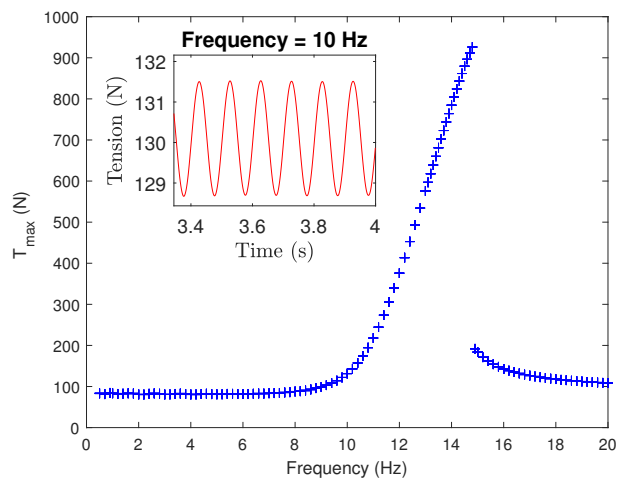


Figure 8. Maximum values of the tension at $s = 0$ versus the forcing frequency in the simulations. The inset shows the evolution of the tension at $s = 0$ for the forcing frequency $f_1 = 10\text{Hz}$.

400 6 Conclusions

The results of this work showed that the proposed model based on Cosserat theory is appropriate for getting insight into the dynamic of the helical structure of a RAWE machine. It offers some advantages as compared to previous models with a large set of masses linked with springs and dampers. For instance, the theory provides a couple of nonlinear partial differential equations that can be solved with well-known numerical methods like the finite element method used in this work. Such a 405 compact formulation, which captures stretching, bending and torsional effects, highlights the role of the different terms on the dynamics of the structure and their coupling. It has also been used here to estimate the characteristics times for the propagation of longitudinal, lateral, and torsional waves in the helix. Moreover, the airborne rotor and the ground-generator enter in the 410 model as boundary conditions that include the position and velocity of the end sections of the structures and the external torque applied to them. The model was completed with the axial, bending, and torsional stiffness of a real AWE machine obtained by conducting three experiments in the laboratory. The relation between the bending and the torsional stiffness and the tension was measured for the tensegrity structure.

The analysis of the stationary solution with no torsion and fixed ends, which was found independently by using a shooting algorithm, allowed to verify the correct implementation of the finite element code. A linear stability analysis was performed to identify longitudinal, lateral, and torsional modes and their natural periods. The quickest mode of the RAWE machine of 415 the company SomeAwe corresponds to a longitudinal mode with period 0.03 s, whereas lateral and torsional modes exhibits



natural oscillations with 0.2 s and 0.4 s. Simple estimations based on classical results for beams are in agreement with these results and constitute a second test for the correct implementation of the code.

The simulation tool provided interesting information about the nominal operation of the RAWE machine. Firstly, a numerical analysis was carried out by keeping fixed the two end points of the structure. It assumed that the rotor imposes a time-dependent 420 external torque that approaches to 25 Nm, which is a typical value for the RAWE machine under consideration. It was shown that a simple proportional-derivative controller for the torque at the ground generator can stabilize the angular spinning velocity of the structure at the target value (120 rpm). For this configuration, the tension is almost constant in time and throughout the structure. However, ~~and~~ although an auxiliary kite is used to anchor the rotor, in a real RAWE machine the upper end point is not fixed due to wind velocity fluctuations and the dynamic coupling of the structure and the rotor. This scenario was mimicked 425 by imposing a circular periodic motion to the upper end of the structure with a forcing frequency f_1 and small amplitude. The experimental and simulation work revealed that there is a resonance that, in the case of the experiment, resulted into the collapse of the structure for a frequency of 5 Hz. The simulator captured essential features of the experiment, like the resonance and the order of magnitude of the critical frequency, but its capability to make accurate quantitative predictions is limited.

Code availability. The code presented in this work was added as an independent module to the open-source software LAKSA.

430 *Author contributions.* The model of the RAWE machine was developed by GSA and ACV. The implementation of the code, the numerical analysis and the preparation of the manuscript were performed by GSA. DU and CB performed the experiments to characterize the RAWE machine in static and dynamic conditions. All the authors contributed to the discussion of the results and the final version of the manuscript.

Competing interests. GSA, ACV and DU declare that they have no conflict of interest. CB is the founder and owner of someAWE Labs.

435 *Acknowledgements.* This work was carried out under the framework of the GreenKite-2 project (PID2019-110146RB-I00) funded by MCIN/AEI/10.13039/501100011033.



References

Archer, C. L. and Caldeira, K.: Global Assessment of High-Altitude Wind Power, *Energies*, 2, 307–319, <https://doi.org/10.3390/en20200307>, 2009.

Beaupoil, C.: Rotary Airborne Wind Energy Systems with Ground Based Power Generation: Overview and Practical Experiences, in: Airborne Wind Energy Conference 2017, edited by Diehl, M., Leuthold, R., and Schmehl, R., p. 133, <https://doi.org/10.6094/UNIFR/12994>, 2017.

Beaupoil, C.: Airborne Wind Energy System with Tensile Rotary Power Transmission test run, <https://www.youtube.com/watch?v=54zM3RC1Xoo&t=96s>, accessed: 2022-10-29, 2022.

440 Benhaiem, P. and Schmehl, R.: Airborne Wind Energy Conversion Using a Rotating Reel System, *Green Energy and Technology*, pp. 539–577, https://doi.org/10.1007/978-981-10-1947-0_22, 2018.

Blanch, M., Makris, A., and Valpy, B.: Getting airborne – the need to realise the benefits of airborne wind energy for net zero, White Paper for Airborne Wind Europe, pp. 1–44, 2022.

Buckham, B. J.: Dynamics Modelling of Low-Tension Tethers for Submerged Remotely Operated Vehicles, Ph.D. thesis, B. Eng. University of Victoria,, 2003.

450 Cherubini, A., Papini, A., Vertechy, R., and Fontana, M.: Airborne Wind Energy Systems: A review of the technologies, *Renewable and Sustainable Energy Reviews*, 51, 1461–1476, <https://doi.org/10.1016/j.rser.2015.07.053>, 2015.

De Schutter, J., Leuthold, R., and Diehl, M.: Optimal Control of a Rigid-Wing Rotary Kite System for Airborne Wind Energy, in: 2018 European Control Conference, pp. 1734–1739, european Control Conference (ECC), Limassol, Cyprus, Jun 12-15, 2018, 2018.

European Commission: Study on challenges in the commercialisation of airborne wind energy systems, 2018.

455 Love, A.: A Treatise on the Mathematical Theory of Elasticity, no. v. 1 in A Treatise on the Mathematical Theory of Elasticity, University Press, 1892.

Mackertich, S. and Das, T.: A quantitative energy and systems analysis framework for airborne wind energy conversion using autorotation, in: 2016 American Control Conference (ACC), pp. 4996–5001, <https://doi.org/10.1109/ACC.2016.7526145>, 2016.

460 Malz, E. C., Walter, V., Goransson, L., and Gros, S.: The value of airborne wind energy to the electricity system, *Wind Energy*, 25, 281–299, <https://doi.org/10.1002/we.2671>, 2022.

Motro, R.: Tensegrity: Structural Systems for the Future, Butterworth-Heinemann, 2003.

Njiri, J. G. and Soffker, D.: State-of-the-art in wind turbine control: Trends and challenges, *Renewable and Sustainable Energy Reviews*, 60, 377–393, <https://doi.org/10.1016/j.rser.2016.01.110>, 2016.

465 Pfister, J.-L. and Blondel, F.: Comparing blade-element theory and vortex computations intended for modelling of yaw aerodynamics of a tethered rotorcraft, in: Science of Making Torque from Wind (TORQUE 2020), PTS 1-5, vol. 1618 of *Journal of Physics Conference Series*, <https://doi.org/10.1088/1742-6596/1618/3/032012>, 2020.

Press, W. H., Teukolsky, S. A., Vetterling, W. T., and Flannery, B. P.: Numerical Recipes in FORTRAN (2nd Ed.): The Art of Scientific Computing, Cambridge University Press, USA, 1992.

470 Ramézani, H., Jeong, J., and Feng, Z.-Q.: On parallel simulation of a new linear Cosserat elasticity model with grid framework model assumptions, *Applied Mathematical Modelling*, 35, 4738–4758, <https://doi.org/10.1016/j.apm.2011.03.054>, 2011.

Rancourt, D., Bolduc-Teasdale, F., Bouchard, E. D., Anderson, M. J., and Mavris, D. N.: Design space exploration of gyrocopter-type airborne wind turbines, *Wind Energy*, 19, 895–909, <https://doi.org/10.1002/we.1873>, 2016.



Read, R.: Kite Networks for Harvesting Wind Energy, pp. 515–537, Springer Singapore, Singapore, https://doi.org/10.1007/978-981-10-1947-0_21, 2018.

475 Riahi, A. and Curran, J. H.: Full 3D finite element Cosserat formulation with application in layered structures, *Applied Mathematical Modelling*, 33, 3450–3464, <https://doi.org/10.1016/j.apm.2008.11.022>, 2009.

Rimkus, S. and Das, T.: An Application of the Autogyro Theory to Airborne Wind Energy Extraction, *ASME 2013 Dynamic Systems and Control Conference, DS/CC 2013*, 3, <https://doi.org/10.1115/DS/CC2013-3840>, 2013.

480 Roberts, B. W., Shepard, D. H., Caldeira, K., Cannon, M. E., Eccles, D. G., Grenier, A. J., and Freidin, J. F.: Harnessing High-Altitude Wind Power, *IEEE Transactions on Energy Conversion*, 22, 136–144, <https://doi.org/10.1109/TEC.2006.889603>, 2007.

Salma, V., Friedl, F., and Schmehl, R.: Improving reliability and safety of airborne wind energy systems, *Wind Energy*, 23, 340–356, <https://doi.org/10.1002/we.2433>, 2020.

Schelbergen, M., Kalverla, P. C., Schmehl, R., and Watson, S. J.: Clustering wind profile shapes to estimate airborne wind energy production, *Wind Energy Science*, 5, 1097–1120, <https://doi.org/10.5194/wes-5-1097-2020>, <https://wes.copernicus.org/articles/5/1097/2020/>, 2020.

485 Schmehl, R.: Springer, Singapore, <https://doi.org/10.1007/978-981-10-1947-0>, 2018.

Sommerfeld, M., Doerenkaemper, M., Steinfeld, G., and Crawford, C.: Improving mesoscale wind speed forecasts using lidar-based observation nudging for airborne wind energy systems, *Wind Energy Science*, 4, 563–580, <https://doi.org/10.5194/wes-4-563-2019>, 2019.

Sommerfeld, M., Doerenkaemper, M., De Schutter, J., and Crawford, C.: Impact of wind profiles on ground-generation airborne wind energy system performance, *Wind Energy Science*, 8, 1153–1178, <https://doi.org/10.5194/wes-8-1153-2023>, 2023.

490 Sánchez-Arriaga, G., García-Villalba, M., and Schmehl, R.: Modeling and dynamics of a two-line kite, *Applied Mathematical Modelling*, 47, 473–486, <https://doi.org/10.1016/j.apm.2017.03.030>, 2017.

Sánchez-Arriaga, G., Pastor-Rodríguez, A., Sanjurjo-Rivo, M., and Schmehl, R.: A lagrangian flight simulator for airborne wind energy systems, *Applied Mathematical Modelling*, 69, 665–684, <https://doi.org/10.1016/j.apm.2018.12.016>, 2019.

495 Tulloch, O., Kazemi Amiri, A. M., Yue, H., Feuchtwang, J., and Read, R.: Tensile rotary power transmission model development for airborne wind energy systems, *Journal of Physics Conference Series*, 1618, 032001, <https://doi.org/10.1088/1742-6596/1618/3/032001>, 2020.

Tulloch, O., Yue, H., Kazemi Amiri, A. M., and Read, R.: A Tensile Rotary Airborne Wind Energy System-Modelling, Analysis and Improved Design, *ENERGIES*, 16, <https://doi.org/10.3390/en16062610>, 2023.

van de Kaa, G. and Kamp, L.: Exploring design dominance in early stages of the dominance process: The case of airborne wind energy, *Journal of Cleaner Production*, 321, 128 918, <https://doi.org/10.1016/j.jclepro.2021.128918>, 2021.

500 Villaggio, P.: Mathematical Models for Elastic Structures, Cambridge University Press, 2005.